5

Effect of Baffles on the Flow Hydrodynamics of Dual-Rushton Turbine Stirred Tank Bioreactor

As presented in Chapter 4, the LBM can effectively predict turbulent flow passing through a stationary body in a closed system. The following work reports the extension of LBM application to model the turbulent flow in a complex geometry equipped with rotational objects. In this chapter, numerical simulations are performed to examine the effect of baffles on flow activity in a stirred tank bioreactor fitted with two six-blade Rushton turbines. The simulations are performed for three different geometries of stirred tank reactors, differentiated based on the impeller clearance. The study shows the impact of baffles on all the three employed geometries.

A detailed overview of the flow system is presented in the next section. Our major contributions for this chapter are:

- Investigate the influence of impeller clearance on the flow pattern in the stirred tank reactor equipped with dual-Rushton impellers.
- And, analyzing the impact of presence and absence of baffles on the flow behavior at different impeller clearance

The rest of the chapter is structured as follows: Section 5.1 details the information about the flow system used in the present work. An overview of the simulation methodology is presented in Section 5.2. Section 5.3 discusses the aspects of numerical setup. The numerical results are presented in Section 5.4. Section 5.5 summarizes the chapter.

5.1 FLOW SYSTEM

The simulation has been performed in a stirred tank reactor of standard configuration. It consists of a fully cylindrical tank of diameter, T with a flat base, open on top. The agitation in the reactor has provided with the two-Rushton impeller of diameter, D. The details of the tank geometry and the impeller are presented in Figure 5.1. The water has filled up to a height (H_w) equal to the tank diameter. The Reynolds number (Re), which fully determines the liquid flow behavior, is defined by $Re = \frac{ND^2}{\nu} \approx 40,000$, where N is the rotational speed of the impeller that is fixed at 250 (in rpm), and ν is the kinematic viscosity of the working fluid (i.e., water) [Derksen and Van den Akker, 1999]. The dimensional values are listed in Table 5.1 [Micale *et al.*, 1999]. A similar flow configuration was studied by Micale *et al.* [1999]. using the sliding-grid method with $k-\omega$ turbulence model to resolve the turbulent structures. Moreover, as the analysis explores the influence of baffles on the flow behavior, the simulation was conducted on the identical configuration of the stirred tank reactor, both in the presence and absence of baffles.

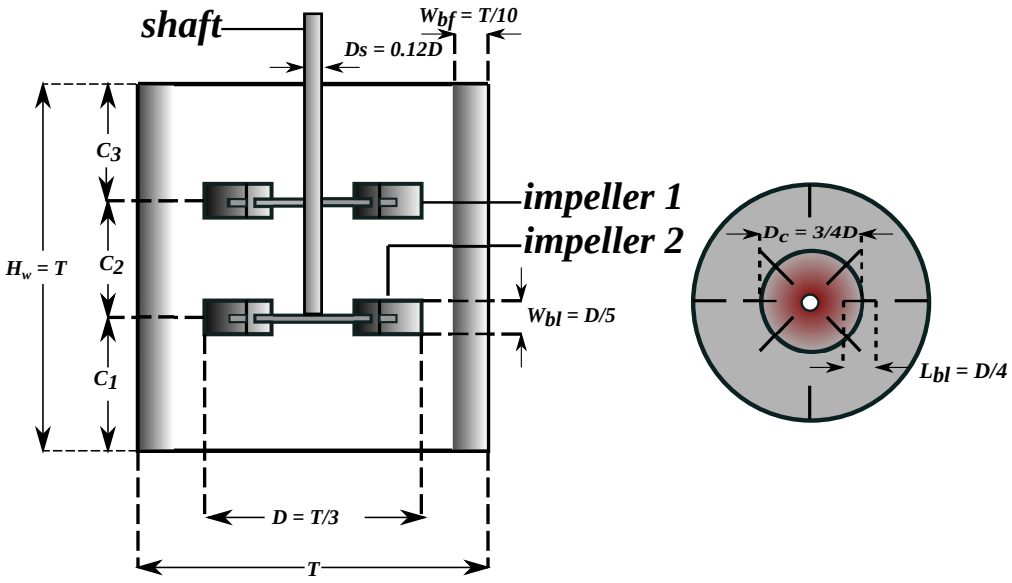

Figure 5.1 : Schematic representation of the flow domain

Table 5.1 : Reactor and impellers dimensions [Rutherford *et al.*, 1996]

	Case 1	Case 2	Case 3
Tank diameter, T (cm)	29.4	29.4	29.4
Water level, H_w (cm)	29.4	29.4	29.4
Water volume, V_w (l)	≈20	≈20	≈20
Baffle width , W_{bf} (cm)	2.94	2.94	2.94
Baffle length, L_{bf} (cm)	29.4	29.6	29.4
Number of baffles plate, N_{bf}	4	4	4
Impeller diameter, D (cm)	9.8	9.8	9.8
Shaft diameter, D_s (cm)	1.176	1.176	1.176
Number of blades, N_{bl}	6	6	6
Circular disk diameter, D_c, (cm)	7.35	7.35	7.35
Blade length, L_{bl} (cm)	2.45	2.45	2.45
Blade width, W_{bl} (cm)	1.96	1.96	1.96
Impeller clearance (cm)	C_1 = 0.25T	C_1 = 0.33T	C_1 = 0.15T
	C_2 = 0.50T	C_2 = 0.33T	C_2 = 0.50T
	C_3 = 0.25T	C_3 = 0.33T	C_3 = 0.35T

5.2 SIMULATION METHODOLOGY

In this work, LBM has been used to discretize the flow domain. The particular lattice Boltzmann (LB) scheme used in the present thesis work is SRT-LBM. The LES is used to model the turbulent flow and the Smagorinsky SGS model is employed to resolve the small-scale turbulent structures. The mathemtical formulation of the SRT-LBM method and the incorporation of LES model in LBM are detailed in Section 3.1.

5.3 ASPECTS OF NUMERICAL SETUP

A uniform, cubic computational grid of 150^3 has been defined for the simulation to discretize the fluid domain. The LES method is used in this analysis to model turbulent flow. For subgrid-closure, the SGS scheme was adopted with a Smagorinsky constant (C_s) of 0.1 [Smagorinsky, 1963]. The particular value of C_s = 0.1 is most commonly used for the shear-driven turbulence [Derksen, 2001]. The no-slip modified bounce-back boundary condition is imposed at the walls of the cube, whereas the free-slip boundary condition is defined at the top surface to represent the free surface, as discussed in Section 3.2. The cylindrical tank wall, the rectangular baffles, the revolving impellers, and the shaft are mounted inside the computational domain. The computational domain of these reactor components is represented as a set of points called control points. The distance between two control points at the reactor components is $0.6\Delta x$, where Δx is the grid spacing equal to $2.0 \times 10^{-3}\ m$. The total number of control points on the impeller surface was 9264, and the number of control points on the cylindrical tank wall was 116,250. The IB-LBM method presented in Section 3.2 is used to model the interaction between the reactor components and the fluid. For cylindrical tank walls and baffles, the boundary nodes have zero velocities. Moving parts are again treated as immersed boundaries but with non-zero velocities. The no-slip condition on the reactor components is maintained by using a two-way coupling approach. In this approach, the surrounding fluid velocity is interpolated onto the control points of the reactor components to measure the force applied by the fluid flow on the boundary surface, and then these forces are distributed back to the surrounding fluid nodes. Moreover, the interpolation between the surrounding fluid nodes and the control points of the reactor components is performed with the cheap-clipped fourth-order polynomial mapping function proposed by Deen *et al.* [2004] as described in Section 4.2. The computer code is developed to efficiently run on the GPU cluster for the execution of the simulations. The details of the implementation of code on the GPU parallel cluster are given in Section 3.3. The simulation starts with a stagnant liquid and proceeds with a time step of 100 μs. The simulation runs for 150,000-time steps, which represent 15s for the operation of the reactor in real-time [Agarwal *et al.*, 2021]. An interested reader, on the other hand, might refer to the major work of Bartels *et al.* [2002] to comprehend memory optimization in parallel-vector computers. The research article used two distinct ways of parallel-vector computing to run numerical simulations on stirred vessel flows at varying Reynolds numbers, one with shared memory and the other with distributed memory.

5.4 RESULTS AND DISCUSSION

The simulations findings demonstrate that the three distinct flow patterns observed rely on the location of impellers, as illustrated in Figure 5.2. Case 1 indicates a parallel flow pattern. Each of the impellers, i.e. upper and lower, generate two vortex rings in their vicinity. Hence, four vortex rings are formed in the parallel flow. The Case 2 shows a merging flow pattern. Here, the flow generated by the impellers merges at a halfway elevation between the upper and lower impeller with a formation of two large vortex rings. A diverging flow pattern is exhibited by Case 3 in which the lower impeller forces the flow stream towards the bottom of the tank. This is attributed to the low position of the impeller. As a result, a large vortex ring is formed near the lower impeller and two vortex rings are formed near the upper impeller.

5.4.1 Instantaneous Flow Field

Figure 5.3-5.5 show contour plots of instantaneous velocity magnitude at the upper impeller location for Case 1, Case 2, and Case 3 respectively, each containing baffles [Agarwal *et al.*, 2021] and without baffles case. For each case comprising baffles, the maximum velocity magnitude is observed near the impeller vicinity, which decreases with an increase in radial distance from the impeller.

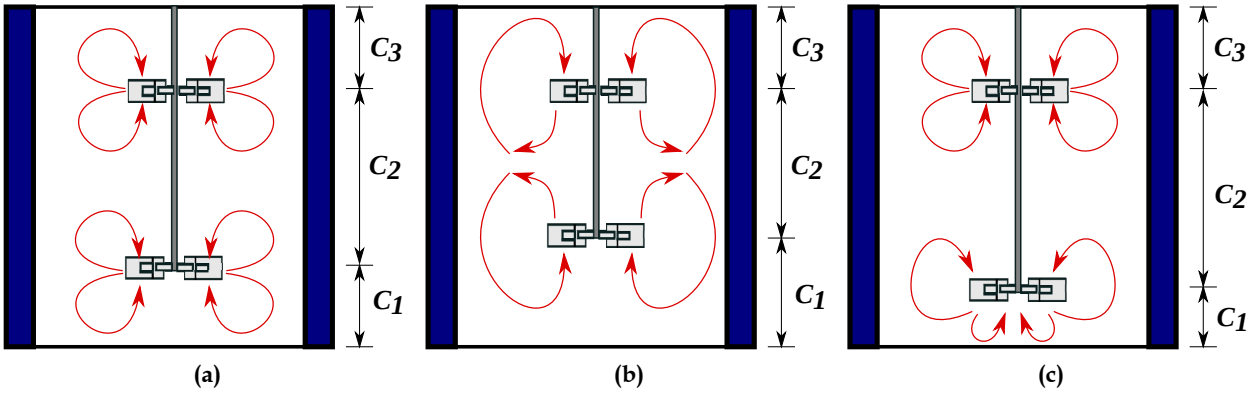

Figure 5.2 : Flow Patterns in the stirred tank reactor with dual-Rushton turbines a) Parallel flow, b) Merging flow, and c) Diverging flow for Case 1, Case 2, and Case 3 respectively in Table 5.1.

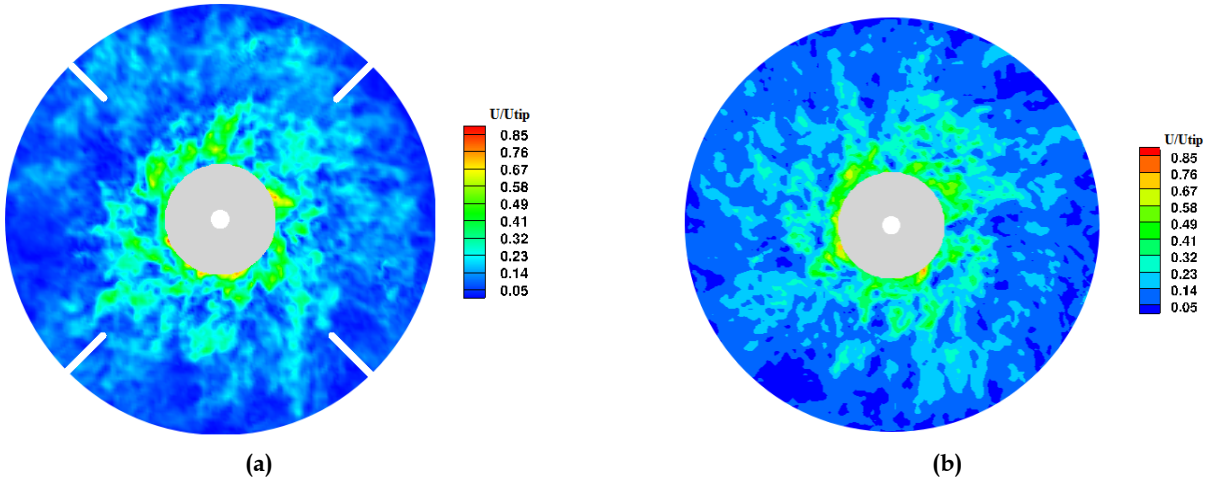

Figure 5.3 : Instantaneous velocity magnitude contour at upper impeller location for Case 1: (a) with baffles, (b) without baffles.

In Case 1, the velocity magnitude shows nearly a similar distribution, i.e., maximum velocity near impeller vicinity and stagnant zone domination near the reactor surface. However, in the Case 2 and Case 3, the situation differs.The velocity magnitude in the instances without baffles is significantly lower than in the baffled cases; this might be due to abrupt abnormalities forming at the tank's surface in the baffled cases. Furthermore, because of the no-slip boundary condition applied on the impeller surface, the greatest velocity magnitude is seen near the reactor surface, resulting in zero relative velocity between the impeller and the fluid particle at the impeller surface. As a result, as the impeller spins, the fluid around it rotates as well, resulting in a greater velocity magnitude closer to the reactor surface.

5.4.2 Phase-Averaged Flow Field

Figure 5.6 shows the contour plots of phase-averaged velocity magnitude at upper impeller location for Case 1, with baffles and without baffles. The phase-averaged velocity is a special

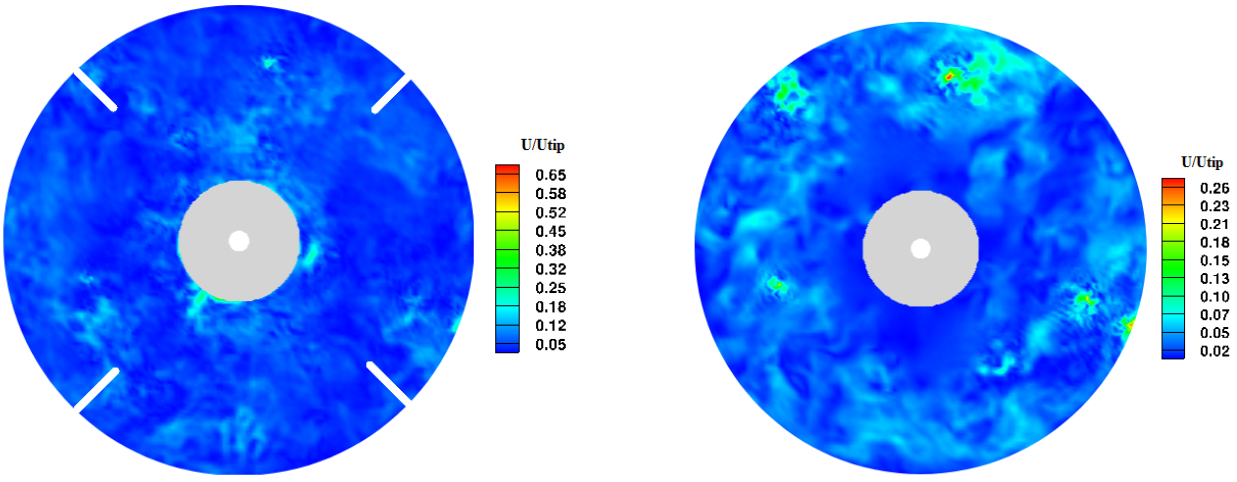

(a) (b)

Figure 5.4 : Instantaneous velocity magnitude contour at upper impeller location for Case 2: (a) with baffles, (b) without baffles.

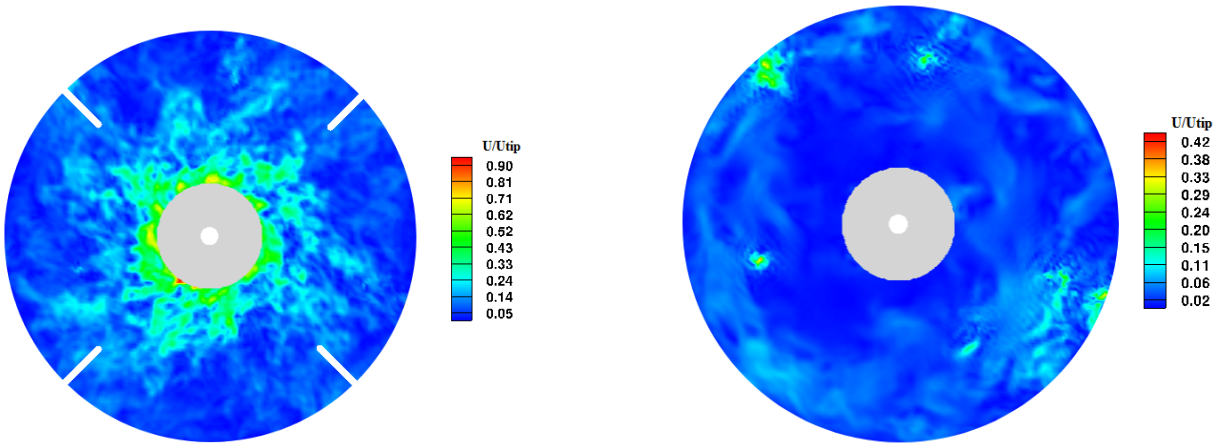

(a) (b)

Figure 5.5 : Instantaneous velocity magnitude contour at upper impeller location for Case 3: (a) with baffles, (b) without baffles.

case of ensemble averaging in which velocity is recorded at the same time during each impeller cycle and then averaged. The maximum phase-averaged velocity magnitude is observed near the impeller tip. Both the velocity contours seem to be identical in terms of velocity magnitude and its distribution. The maximum phase-averaged velocity magnitude is approximately 0.65 times than the linear velocity at the tip of the impeller blades U_{tip} for both the cases, i.e., with and without baffles. The linear tip velocity of the blades is equal to the rotational speed of the impeller (i.e., 250 rpm or 1.28 m/s). Moreover, the present study depicts that the tip velocity of the blades can only be used to make a qualitative estimate of the maximum fluid flow velocity magnitude.

Figures 5.7 and 5.8 show the contour plots of phase-averaged velocity magnitude at upper

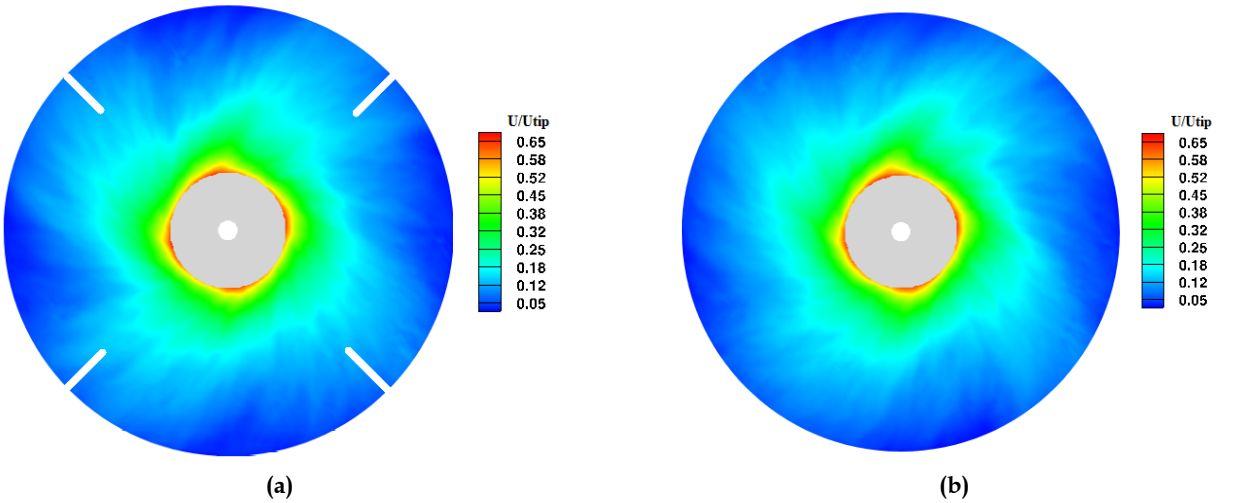

(a) (b)

Figure 5.6 : Phase-averaged velocity magnitude contour at upper impeller location for Case 1: (a) with baffles, (b) without baffles.

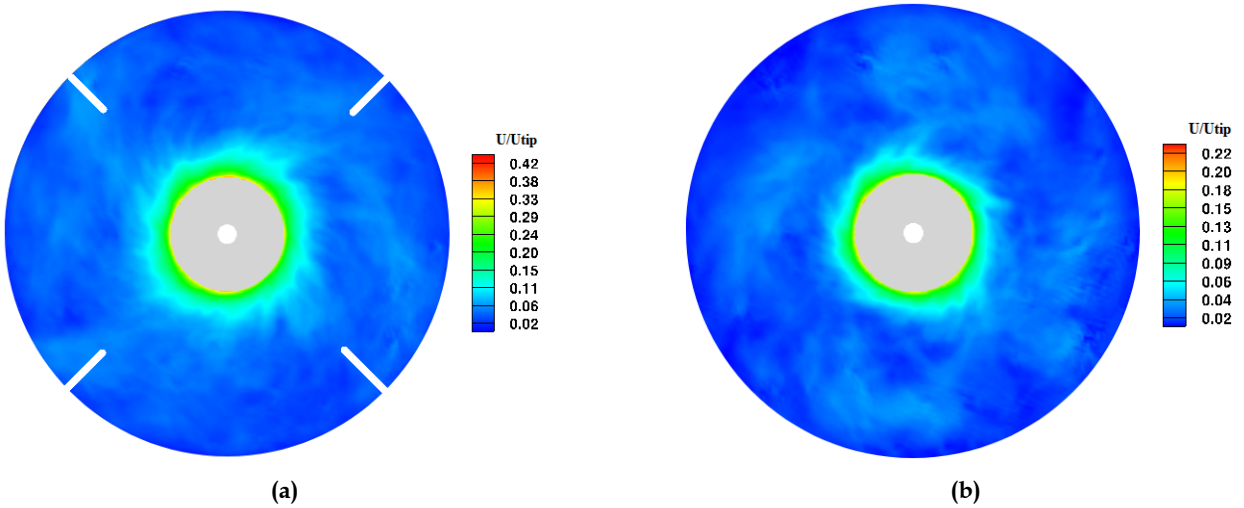

(a) (b)

Figure 5.7 : Phase-averaged velocity magnitude contour at upper impeller location for Case 2: (a) with baffles, (b) without baffles.

impeller location for Case 2 and Case 3 respectively, with baffles [Agarwal *et al.*, 2021] and without baffles. The velocity magnitude at the upper impeller is reduced as compared to the parallel flow. In Figure 5.7, the without baffles case is also showing the same behavior but with a smaller velocity magnitude. The average velocity magnitude is maximum at the impeller vicinity, which reduces towards the reactor surface. The case with baffles shows a higher velocity magnitude with a reduced stagnant zone. In Figure 5.8, the stagnant region is less than that of the above two cases for the without baffles case. As discussed above, the parallel, merging, and diverging flows depend on the distance between the upper and lower impeller blades and the distance between the lower impeller blades from the bottom of the tank. Moreover, as far as the stagnant region area is concerned, it could be due to the strong swirling flow characteristics of Case 3 as compared to

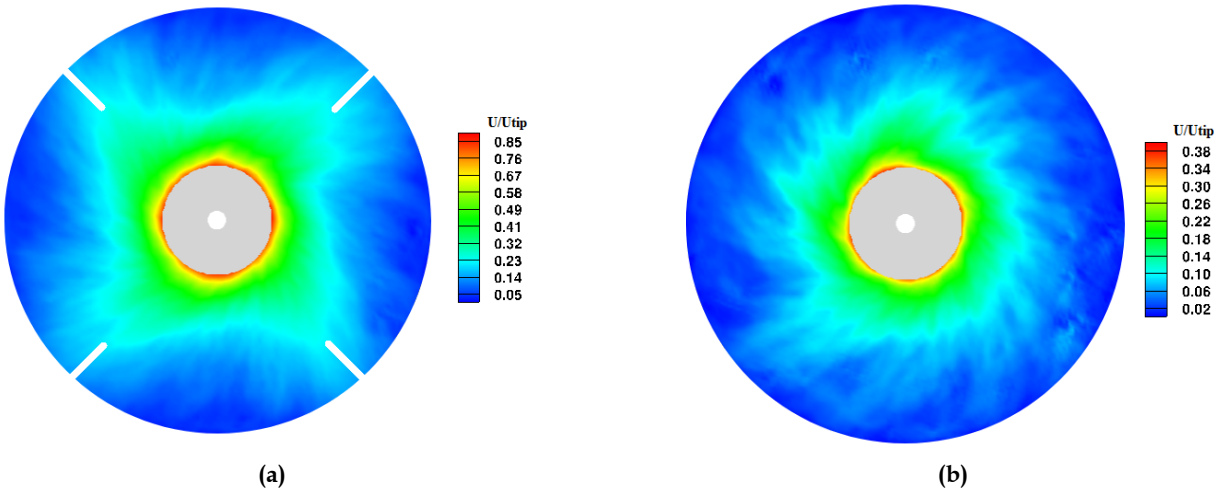

(a) (b)

Figure 5.8 : Phase-averaged velocity magnitude contour at upper impeller location for Case 3: (a) with baffles, (b) without baffles.

Case 1 and Case 2 [Li *et al.*, 2012].

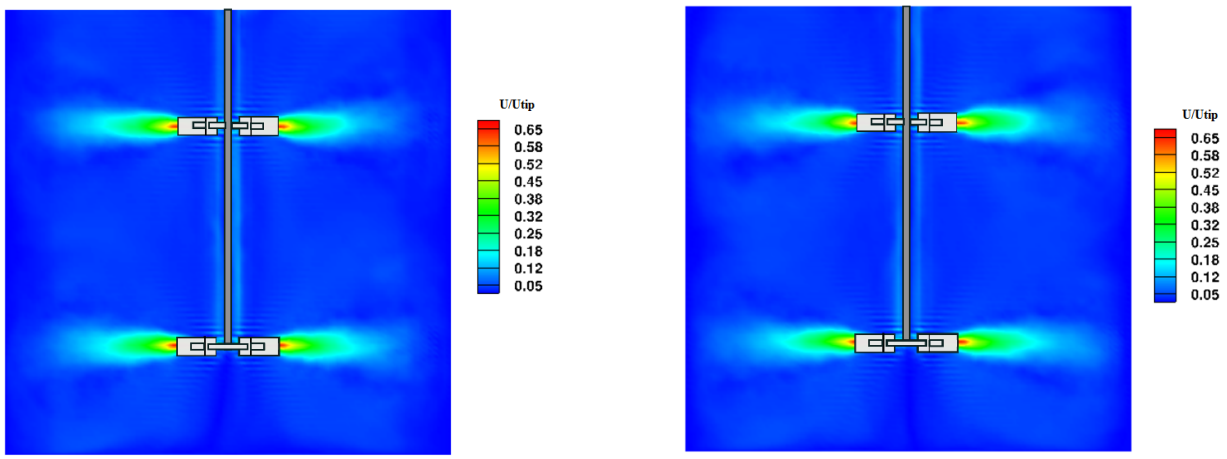

(a) (b)

Figure 5.9 : Phase-averaged velocity magnitude contour at $\theta = 0^{\circ}$ for Case 1: (a) with baffles, (b) without baffles.

Figure 5.9 shows the contour plots of phase-averaged velocity magnitude at θ=0° for Case 1. The maximum velocity magnitude is near the vicinity of both the upper and lower impellers. In both the cases i.e. with and without baffles, the velocity magnitudes are showing the same spread. Most of the contour plot is showing dominance of dead zone or stagnation zone. The stagnant zone is undesirable as the energy dissipation takes place in a smaller volume. In both cases, i.e., with and without baffles, the velocity contours are nearly identical. Nonetheless, the primary purpose of using baffles in the reactor is to avoid the swirl motion of the fluid in agitation. The baffles in the reactor convert the swirl motion of the fluid in the desired flow pattern. It converts the rotational flow of fluid to an axial flow, resulting in proper mixing. However, for the parallel flow bioreactor, the flow pattern for both with and without baffles' cases is similar. Hence bioreactors

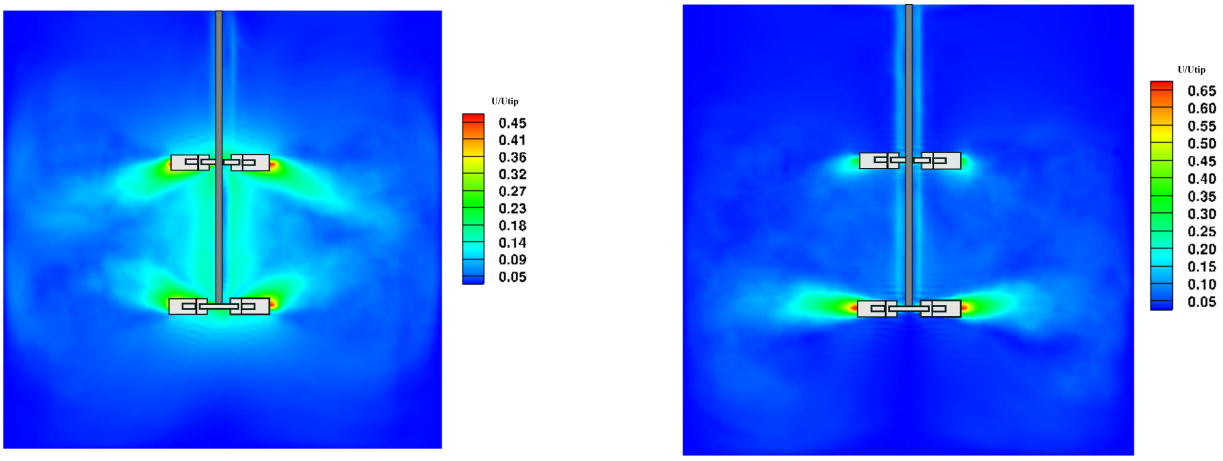

(a) (b)

Figure 5.10 : Phase-averaged velocity magnitude contour at $\theta = 0^\circ$ for Case 2: (a) with baffles, (b) without baffles.

without baffles can be chosen over the baffled bioreactor to reduce the material requirement for its manufacturing. Moreover, by reducing the material requirement, the manufacturing cost of the bioreactor also decreases. Figure 5.10 shows the contour plot of phase-averaged velocity magnitude at θ=0° for Case 2. The vortices are mixing in both the cases, with and without baffles. However, the mixing is stronger in the 'with baffles' case than the 'without baffles' one. The stagnant zone is also reduced in this case as compared to the parallel flow i.e. Case 1. However, the stagnant zone is dominant in the case without baffles. Hence, the case with baffles will exhibit better mixing. Figure 5.11 shows the contour plot of phase-averaged velocity magnitude at θ=0° for Case 3 [Agarwal *et al.*, 2021]. The development of vortex can be seen at the bottom having a good spread. It is desirable in terms of mixing. However, the mixing of upper and lower vortices is not observed here. The magnitude of velocity is higher in baffle case but the spread of vortex is better in the latter case. The stagnant zone is reduced as compared to Case 1, especially at the bottom side of the reactor.

Figure 5.12 shows the comparison of axial profiles of phase-averaged radial velocity in a plane midway between baffles at different radial locations for Case 1. The simulation results are compared with the experimental data of Rutherford *et al.* [1996]. The results are in excellent agreement with the experimental data and seem nearly overlapping at all the radial positions considered for the simulations. The effect of baffles is not significant, and the axial velocity profiles for all the radial positions are following the same profile.

Similarly, the comparison of axial profiles of phase-averaged radial velocity in a plane midway between baffles at different radial locations for Case 2 is shown in Figure 5.13. The results are showing a similar trend away from the impellers but near the vicinity of the impeller, the LBM results slightly under predict the experimental measurements. The 'without baffles' case is quite unable to predict the velocity profile, especially near the upper impeller at all the radial positions. The double-peak shape is not exhibited by the simulations without baffles. Figure 5.14 shows the comparison of axial profiles of phase-averaged radial velocity in a plane midway between baffles at different radial locations for Case 3 [Agarwal *et al.*, 2021]. The 'with baffles' simulation cases are slightly over predicting the experimental measurements near the impeller vicinity. The diverging nature of flow at the bottom impeller can be seen with the increasing radial position. Here, the LBM

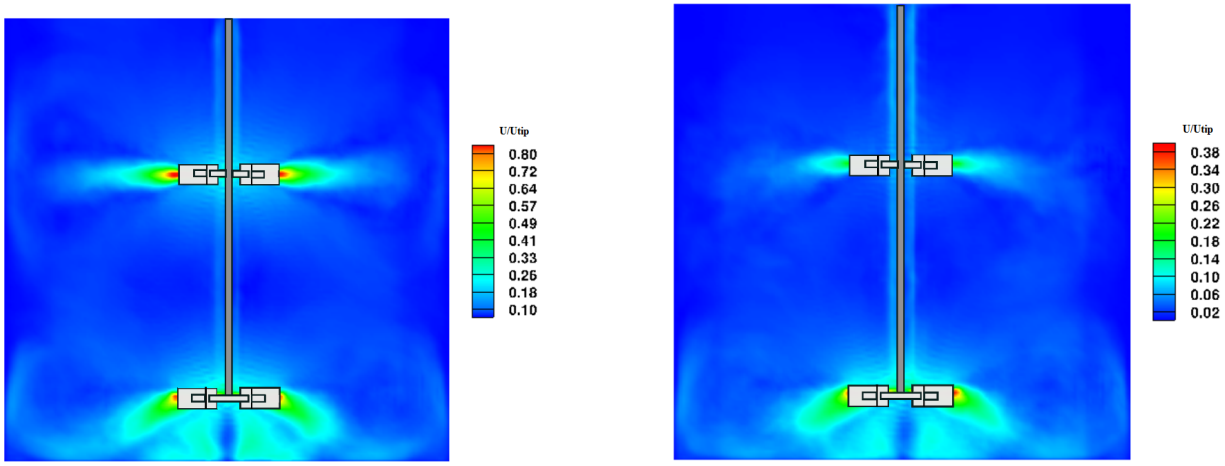

(a) (b)

Figure 5.11 : Phase-averaged velocity magnitude contour at $\theta = 0^{\circ}$ for Case 3: (a) with baffles, (b) without baffles.

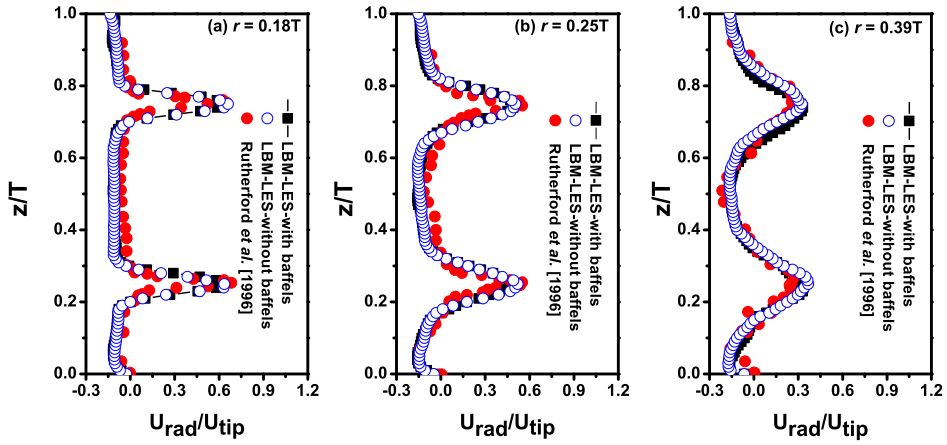

Figure 5.12 : Comparison of axial profiles of phase-averaged radial velocity in a plane midway between baffles at different radial locations for Case 1.

simulations for the 'with baffles' cases are showing better agreement with the experimental data. Additionally, the 'without baffles' case is also simulated for a comparison which shows a lower velocity magnitude at the upper impeller location for all the radial positions. This could be due to the placement of the impellers. The lower impeller of Case 3 is located close to the bottom of the tank, and the distance of the upper impeller from the top of the water level is more comparable to the other two cases (Case 1 and 2). It results in strong swirling flow characteristics for Case 3, and the presence of baffles breaks the swirling flow that leads to increased turbulence at all the radial locations of the upper impeller, resulting in higher velocity magnitude. However, the absence of baffles deteriorates the turbulence level, which in turn decreases the velocity magnitude.

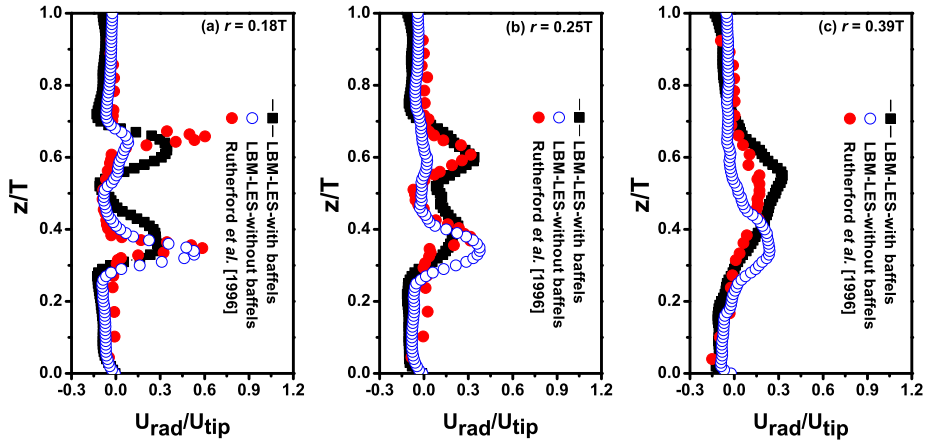

Figure 5.13 : Comparison of axial profiles of phase-averaged radial velocity in a plane midway between baffles at different radial locations for Case 2.

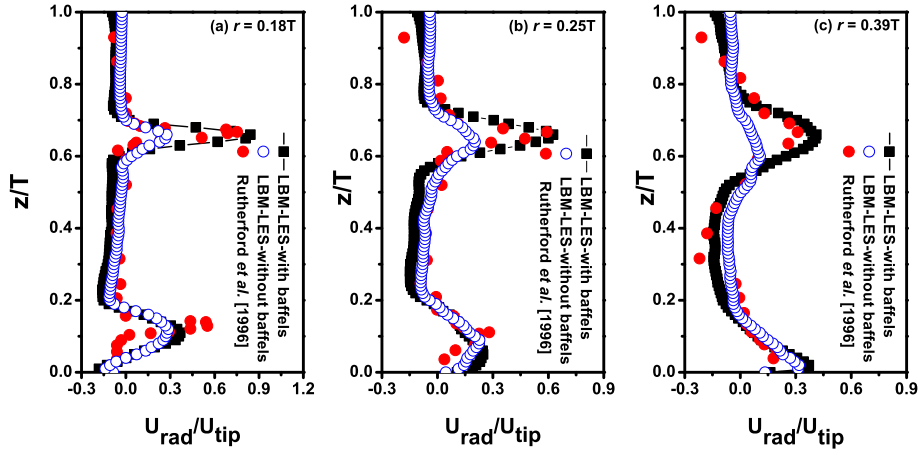

Figure 5.14 : Comparison of axial profiles of phase-averaged radial velocity in a plane midway between baffles at different radial locations for Case 3 [Agarwal *et al.*, 2021].

5.4.3 Turbulent Kinetic Energy

Figure 5.15 shows the comparison of axial profiles of TKE in a plane midway between baffles at different radial locations for Case 1. As shown in Figure 5.15, the kinetic energy is maximum at the impeller tips due to high-velocity magnitude. Both the 'with and without baffles' cases are slightly over-predicting the turbulent kinetic energy compared to the experimental data, especially at the smaller radial position. As the radial position increase, the results match with a relatively lower deviation than before.

Similarly, for Case 2 as shown in Figure 5.16, the double peaks are observed for the baffles case at the radial location close to the impellers. The results are in good comparison with the experimental data. Moreover, the without baffles case under-predicated the turbulent kinetic energy at the upper impeller; however, at the lower impeller, results are slightly over-predicted. Furthermore, at the radial location away from the impellers locations, the with baffles case are in

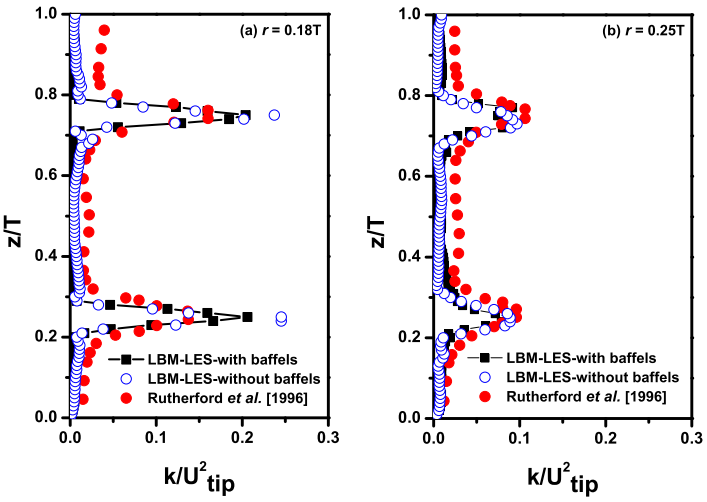

Figure 5.15 : Comparison of axial profiles of turbulent kinetic energy in a plane midway between baffles at different radial locations for Case 1.

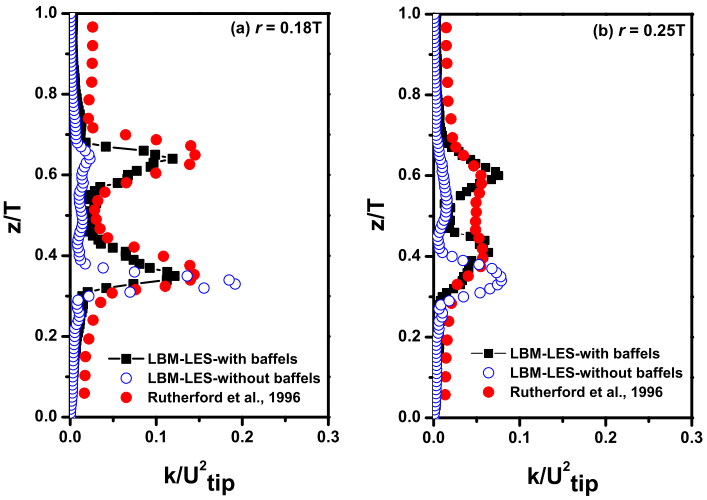

Figure 5.16 : Comparison of axial profiles of turbulent kinetic energy in a plane midway between baffles at different radial locations for Case 2.

close agreement with the experimental results, except in the region between the two impellers, and without baffles case shows similar under-predication at the upper impeller, and a slight shift is observed in the peak at the lower impeller. In Case 3, the double peaks are exhibited near the impellers. However, the simulation results are slightly over-predicting the experimental data, especially near the upper impeller. The without baffles case also shows nearly a similar behavior near the lower impeller, but the turbulent kinetic energy has less magnitude near the upper impeller. Among the three cases, Case 1, i.e., parallel flow, depicts nearly the similar profile of velocity magnitudes and turbulent kinetic energy for both the simulation cases of with and without baffles and are in excellent agreement with the experimental data.

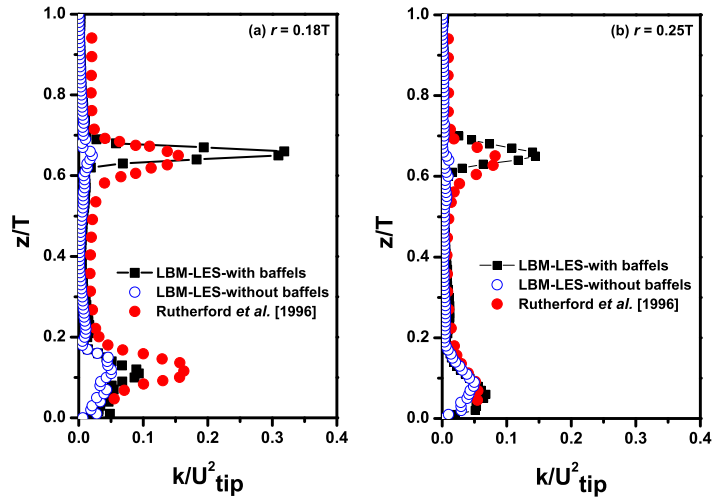

Figure 5.17 : Comparison of axial profiles of turbulent kinetic energy in a plane midway between baffles at different radial locations for Case 3

5.5 SUMMARY

The chapter presented an overall framework to scrutinize the effects of baffles on the flow hydrodynamics of the stirred tank reactor equipped with dual-Rushton turbines at different impeller clearance. The study reported the results for the placement of impellers at different locations along with the presence and absence of baffles in the reactor. The study used LBM as a numerical approach to discretize the fluid domain. LES is used to model the turbulent flow, and small-scale turbulent structures are resolved by the Smagorinsky SGS model. The obtained results are compared and validated with the experimental findings reported in the literature. The results show a good agreement between the reported experimental data and the performed simulations using the LBM-LES model. The results show that in the absence of baffles, the magnitude of instantaneous velocity, phase averaged velocity, and turbulent kinetic energy is less for diverging and merging flow in the absence of baffles. One interesting finding of this study revealed that the presence or absence of baffles does not affect the velocity and turbulent kinetic energy in the parallel flow arrangement. It affirms that the baffled design can be avoided in the case of parallel flow to reduce manufacturing costs and save material. The outcomes presented in this chapter demonstrated that LBM, along with the modeling of turbulent flow past over a stationary object in a closed system, is also suitable to accurately predict the turbulent flow behavior in complex geometry equipped with rotational components.

…